

Low-Mass Galaxy Interactions Trigger Black Hole Activity

MARKO MIĆIĆ ¹, JIMMY A. IRWIN ², PREETHI NAIR ², BRENNAN N. WELLS ³, OLIVIA J. HOLMES ⁴ AND JACKSON T. EAMES ²

¹*Homer L. Dodge Department of Physics and Astronomy, The University of Oklahoma, Norman, OK 73019, USA*

²*Department of Physics & Astronomy, University of Alabama, Tuscaloosa, AL 35401, USA*

³*Department of Physics, Duke University, Durham, NC 27708, USA*

⁴*Department of Physics and Astronomy, Purdue University, West Lafayette, IN 47907, USA*

ABSTRACT

The existence of high- z over-massive supermassive black holes represents a major conundrum in our understanding of black hole evolution. In this paper, we probe from the observational point of view how early Universe environmental conditions could have acted as an evolutionary mechanism for the accelerated growth of the first black holes. Under the assumption that the early Universe is dominated by dwarf galaxies, we investigate the hypothesis that dwarf-dwarf galaxy interactions trigger black hole accretion. We present the discovery of 82 dwarf-dwarf galaxy pairs and 11 dwarf galaxy groups using the Hubble Space Telescope, doubling existing samples. The dwarf systems span a redshift range of $0.13 < z < 1.5$, and a stellar mass range of $7.24 < \log(M_*/M_\odot) < 9.73$. We performed an X-ray study of a subset of these dwarf systems with Chandra and detected six new AGN, increasing the number of known dwarf-dwarf-merger-related AGN from one to seven. We then compared the frequency of these AGN in grouped/paired dwarfs to that of isolated dwarfs and found a statistically significant enhancement (4σ - 6σ) in the interacting sample. This study, the first of its kind at the lowest mass scales, implies that the presence of a nearby dwarf neighbor is efficient in triggering black hole accretion. These results open new avenues for indirect studies of the emergence of the first supermassive black holes.

Keywords: Active galactic nuclei (16) — Dwarf galaxies (416) — Galaxy mergers (608) — Supermassive black holes (1663)

1. INTRODUCTION

Observations of high redshift quasars suggest that supermassive black holes, billions of times more massive than our Sun, were already in place less than 700 million years after the Big Bang (Bogdán et al. 2024; Wang et al. 2021; Bañados et al. 2018; Yang et al. 2020). The formation and growth paths of these black holes are largely unexplored and remain in the domain of speculation (Loeb & Rasio 1994; Madau & Rees 2001; Bromm & Loeb 2003). One of the mechanisms that can be responsible for triggering the active galactic nuclei (AGN) and subsequent black hole growth is galaxy interactions.

Various observational, computational, and theoretical works tried to establish the link between galaxy interactions and black hole activity. Prieto et al. (2021) used hydrodynamical simulations to demonstrate that gravitational and hydrodynamical torques near pericenter passes trigger black hole growth and bursts of black hole accretion that approach Eddington limits. Gao et al. (2020) studied galaxy mergers up to redshift $z=0.6$ and found that they play a non-negligible to potentially significant role in AGN triggering. Li et al. (2023) studied the post-merger remnant galaxies and found that they are two to four times more likely to host an AGN when compared to non-interacting galaxies. On the other hand, Silva et al. (2021) studied mergers of the most massive galaxies and concluded that in the most massive regime, mergers do not play a significant role in AGN activation. However, none of these works probed

populations of galaxies that are prevalent in the early Universe.

Observations of the ultraviolet luminosity function imply that beyond $z=8$ an unseen population of low-mass galaxies overwhelmingly dominates the galaxy population, and as a result dominates the merger rate per unit volume (Mason et al. 2015). Recent James Webb Space Telescope observations confirmed this hypothesis by discovering that faint dwarf galaxies played a major role in ionizing the Universe during the first billion years (Atek et al. 2024). Even though these high- z low-mass galaxies are beyond our reach, using local dwarf galaxies as high- z analogs and establishing the relationship between dwarf-dwarf interactions and black hole accretion can provide vital clues for understanding how the first black holes evolved and acquired mass.

However, only a small number of dwarf-dwarf galaxy pairs and dwarf galaxy groups have been detected in large-scale surveys (Stierwalt et al. 2015; Paudel et al. 2018; Stierwalt et al. 2017), and none of them have been reported to have an AGN. Aside from these large-scale surveys, only one confirmed AGN in a dwarf-dwarf merger is known in the whole Universe (Reines et al. 2014; Kimbro et al. 2021), and two more dual AGN in dwarf-dwarf mergers have been identified as viable candidates (Mićić et al. 2023). The lack of a comprehensive survey for AGN in dwarf-dwarf mergers makes investigating the early stages of black hole evolution a non-trivial task.

2. DATA

In this paper, we used the data derived from the 3D-HST survey, a 248-orbit HST Treasury program (Momcheva et al. 2016; Skelton et al. 2014). It covers all five CANDELS fields and provides information on distance (spectroscopic or photometric), stellar masses, star formation rates, and stellar ages for over 200,000 galaxies. The survey performed the WFC3/G141 grism spectroscopy, yielding precise distance estimates and emission line measurements for $\sim 22,000$ galaxies. The accuracy of obtained redshifts was evaluated by comparing them to the available ground-based spectroscopic redshifts. It was found that there is an excellent overall agreement between the two samples. However, the accuracy of individual redshifts might be affected by distance, magnitude, color, or star-formation rate. Stellar masses, and other stellar properties, are derived using the FAST code, assuming the Bruzual & Charlot (2003) stellar population synthesis model, Chabrier (2003) initial mass function, solar metallicity, and exponentially declining star formation histories. For more detailed information, we refer the reader to Skelton et al. (2014).

The CANDELS deep fields contain an abundance of existing multiwavelength coverage allowing an in-depth search for AGN. Nevertheless, detecting AGN in dwarf galaxies is notoriously challenging. Since X-ray emission is ubiquitous in AGN, most past works used X-ray observatories to uncover dwarf AGN (Lemons et al. 2015; Pardo et al. 2016; Mezcuca et al. 2016; Birchall et al. 2020). However, lower-mass galaxies are expected to host lower-mass central black holes that are expected to be dim in X-rays, often requiring hundreds of kiloseconds to detect them even at modest distances (Simmonds et al. 2016). For that reason, we focus on the GOODS-South field, where the deepest Chandra X-ray observations exist. The GOODS-South field was observed with Chandra 102 times between October 1999 and March 2016, for a total exposure time of 7 megaseconds. The unprecedented depth providing extreme sensitivity coupled with superior angular resolution, makes Chandra an ideal tool to search for dwarf AGN in the GOODS-South field. With the large spread in redshifts in galaxies from the 3D-HST sample, the X-ray detection limits vary greatly. However, throughout the sample, we can probe low luminosity AGN (LLAGN) up to some extent. The detection of LLAGN is important for the completeness of our study because simulations suggest that AGN luminosity is variable on different timescales throughout the merger. The AGN remain in the low-luminosity state ($L_{bol} < 10^{42}$ erg s^{-1}) for $\sim 1-2$ gigayears (Hopkins et al. 2008), significantly longer than in the high-luminosity state ($L_{bol} > 10^{42}$ erg s^{-1}), in which they are expected to spend only $\sim 1-10$ megayears (Hopkins & Hernquist 2009). Therefore, a study unable to probe LLAGN would not achieve an acceptable census of merger-triggered AGN.

3. RESULTS

3.1. Dwarf-dwarf pairs and dwarf groups

We surveyed the publicly available galaxy catalogs from the 3D-HST Survey, consisting of objects residing in GOODS-South, GOODS-North, AEGIS, UDS, and COSMOS deep fields (Momcheva et al. 2016; Skelton et al. 2014). We selected all galaxies with spectroscopically confirmed redshifts and stellar masses less than $\log(M_*/M_\odot) < 9.75$ ($\sim 5 \times 10^9 M_\odot$), resulting in 1663 dwarf galaxies. We then examined the environments of each galaxy, looking for those dwarfs that only had another dwarf companion within $\Delta z = 0.002$ and 100 kpc in the projected distance. The Δz criterion reflects a very conservative assumption of redshift uncertainty, while the projected separation criterion corresponds to an approximate virial radius of a dwarf galaxy (Stierwalt et al. 2015). We classify our dwarf systems in five different

groups: (1) confirmed dwarf-dwarf pairs, where both dwarfs have spectroscopic redshifts; (2) candidate dwarf-dwarf pairs, where one galaxy has a spectroscopic redshift, while the other has a photometric redshift; (3) confirmed dwarf galaxy groups, where three or more dwarfs have spectroscopic redshifts; (4) confirmed dwarf pairs but potential dwarf groups, where two dwarfs have spectroscopic redshifts and one or more additional galaxies have photometric redshifts; (5) candidate dwarf groups, where one galaxy has a spectroscopic redshift and two or more dwarfs have photometric redshifts. This procedure resulted in the discovery of 82 new dwarf-dwarf galaxy pairs and 11 new dwarf galaxy groups, approximately doubling existing samples.

3.2. Demographics of dwarf systems

The environment of every dwarf galaxy was carefully examined, primarily looking for spectroscopically confirmed dwarf neighbors. However, we also looked for nearby dwarfs with matching photometric redshifts, constituting potential dwarf pairs and groups. This procedure resulted in 51 spectroscopically confirmed dwarf pairs, 31 potential dwarf pairs, 8 spectroscopically confirmed dwarf groups, and 3 potential dwarf groups. Out of 93 dwarf systems, 40 ($\sim 43\%$) reside in the GOODS-N field, 29 ($\sim 31.2\%$) reside in the GOODS-S field, 17 ($\sim 18.3\%$) reside in the AEGIS field, 6 ($\sim 6.5\%$) reside in the COSMOS field, and 1 ($\sim 1\%$) resides in the UDS field. The field distribution of dwarf systems roughly follows the distribution of the parent dwarf sample. Our dwarf systems span a wide range of redshifts, $0.127 < z < 1.486$, projected separations $3 \text{ kpc} < r_{sep} < 93 \text{ kpc}$, stellar masses $7.24 < \log(M_*/M_\odot) < 9.73$, and mass ratios $1 < M_{1*}/M_{2*} < 26$. Such a diverse sample will be of essential importance for future comparative studies of various drivers of different aspects of galactic evolution. The summary of properties of all dwarf systems is given in Tables 1 through 3. The demographics of dwarf systems is graphically represented in Figure 1. A selected subsample of dwarf systems is shown in Figure 2.

3.3. X-ray analysis

We crossmatched all dwarf galaxies from the GOODS-South dwarf systems with the Chandra X-ray Catalog (Evans et al. 2010) and found seven X-ray sources within $1''$ from the host dwarf. The X-ray sources reside in dwarf systems labeled as id3, id10, id34, id43, id81, id86, and id91 in Table 1 through Table 3. Observed fluxes in the 0.3-7 keV band vary from 1×10^{-14} to 3×10^{-17} erg s $^{-1}$ cm $^{-2}$. The X-ray luminosities were calculated using reported fluxes and adopting the redshift of the

host galaxy as distance:

$$L_X = 4\pi d_L^2 f_X \quad (1)$$

where d_L is the luminosity distance in centimeters and f_X is X-ray flux, and then converted to rest-frame 0.5-10 keV luminosities assuming a model with a typical AGN power law of $\Gamma=1.9$ and accounting for the appropriate K-correction factor. The luminosities range from 2×10^{40} to 3×10^{43} erg s $^{-1}$. We note that six out of seven X-ray sources have luminosities $< 10^{42}$ erg s $^{-1}$, in line with LLAGN. Such low luminosities do not necessarily have to be produced by an accreting supermassive black hole. For example, the hot interstellar medium (ISM) gas and unresolved populations of X-ray binaries (XRBs) can produce LLAGN-similar levels of X-ray emission. Thus, we evaluate the non-AGN contributions to the observed X-ray flux.

For the X-ray binary contribution, we use the relation from Lehmer et al. (2016) that is based on a sample of normal galaxies at redshifts $z \sim 0-7$:

$$L_{2-10\text{keV}}^{\text{XRB}} = \alpha_O(1+z)^\gamma M_* + \beta_0(1+z)^\delta \text{SFR} \quad (2)$$

in erg s $^{-1}$, where $\log \alpha_O = 29.30 \pm 0.28$, $\log \beta_0 = 39.40 \pm 0.08$, $\gamma = 2.19 \pm 0.99$, $\delta = 1.02 \pm 0.22$, M_* is stellar mass, and SFR is star formation rate in units of $M_\odot \text{ yr}^{-1}$. The M_* term is proportional to low-mass XRBs, while the SFR term is proportional to high-mass XRBs. These luminosities are then converted to the 0.5-10 keV energy band assuming a $\Gamma=1.4$ model (Hickox & Markevitch 2006) and applying appropriate K-correction factor. We find that one X-ray source, id81, is in line with the expected emission from the XRB population. On the other hand, the X-ray source from id43, the only non-LLAGN source, exceeds the expected XRB contribution by a factor of ~ 500 . In the remaining five sources, the XRB contributions account for 4%-22% of the observed X-ray emission, with a median value of 16%, requiring an additional source of intensive X-ray emission. However, this relation was derived considering all galaxies with $L_X < 3 \times 10^{42}$ erg s $^{-1}$ to be non-AGN star-forming galaxies. An overwhelming majority of known X-ray-detected dwarf AGN, including six out of seven of our sources, have luminosities lower than this value and would be classified as non-AGN galaxies in the computation of Lehmer et al. (2016) relation.

Another scaling relation between XRB emission, M_* , and SFR is derived by Lehmer et al. (2010) using a sample of luminous star-forming galaxies:

$$L_{2-10\text{keV}}^{\text{XRB}} = (9.05 \pm 0.37) \times 10^{28} M_* + (1.62 \pm 0.22) \times 10^{39} \text{SFR} \quad (3)$$

Even though this relation yields lower XRB contributions, the overall results remain the same. One X-ray source, id81, is consistent with the XRB emission; the only non-LLAGN source, id43, exceeds the XRB predicted emission by a factor of 1500; and in the other five sources, the XRB contributions are expected to account for 0.6%-12% with a median value of 5%. We note that various other relations for estimating the XRB emission exist (e.g. [Fragos et al. 2013](#); [Lehmer et al. 2022](#)) which may yield different values for the XRB contributions, but the overall conclusions remain the same.

We estimate the 0.5-2 keV hot ISM gas X-ray luminosity using the relation from [Mineo et al. \(2012\)](#):

$$L_{0.5-2\text{keV}}^{\text{hot}} = (8.3 \pm 0.01) \times 10^{38} SFR \quad (4)$$

The resulting luminosities are converted to a 0.5-10 keV energy band assuming a power-law index $\Gamma=3$ and using an appropriate K-correction factor. We find that the ISM X-ray emission plays a minor role as it accounts for a fraction of a percent up to a few percent of observed X-ray emission.

Therefore, we find that in one case, id81, the expected XRB contribution to the X-ray emission exceeds the observed X-ray emission, thus, the presence of an AGN is unlikely and id81 is removed from the final AGN sample. In the remaining six sources we find sufficient evidence for AGN presence. The total X-ray luminosities, XRB and ISM contributions, and calibrated AGN luminosity for each of the six sources are given in Table 4. Dwarf systems hosting the AGN are shown in Figure 3.

3.4. AGN frequency

We note that four out of six of our AGN reside in late-stage galaxy mergers, where galaxies are separated by less than 10 kpc. Due to the large redshifts, the angular separations correspond to $<1''$. This implies that even if the observations were perfectly focused, distinguishing between the two AGN would be a non-trivial task. We find that the smallest off-axis angle is $\sim 2/5$ (id86), and the resulting Chandra point-spread function is greater than the angular separation between the merging galaxies, leaving the possibility of a dual AGN appearing as a single AGN. Various works agree that the dual AGN frequency increases with the decrease of galaxy separation (e.g., [Koss et al. 2012](#); [Barrows et al. 2017](#)), implying that probably some, if not all, of our four late-stage mergers host dual AGN. As a result of this ambiguity, we report two AGN values: the lower AGN limit consisting of six confirmed AGN, $N_{\text{agn,low}}=6$; and the higher AGN limit, assuming that all of the four late-stage mergers host dual AGN, $N_{\text{agn,high}}=10$. The corresponding X-ray AGN frequency per paired/grouped dwarf galaxy

is $9.8\%_{-3.9}^{+5.9}$ in the lower limit, and $16.4\%_{-5.1}^{+7.0}$ in the higher limit, with uncertainties obtained from the Poissonian statistics at 1σ level. ([Gehrels 1986](#)). In follow-up work, we plan to use novel Bayesian tools such as BAYMAX to estimate the likelihood of dual AGN posing as single AGN ([Foord et al. 2019](#)).

3.5. Control sample

The inferred AGN frequency in interacting dwarfs, in either limit, is significantly higher than in any existing work that tackled the problem of dwarf AGN. However, many factors can play a role in different AGN frequencies, the most prominent reasons being redshifts, stellar masses of galaxies examined, and the depth of observations used. To truthfully estimate the magnitude of enhanced black hole accretion (if any) in an interacting sample of dwarf galaxies, we constructed a sample of isolated dwarfs with identical redshift and stellar mass distributions, for which the same depth of X-ray observations are available. Therefore, the interacting dwarfs and control sample dwarfs would be intrinsically more-or-less identical, exposed to the same observational conditions, and the only variable that could cause different AGN frequency would be the environment, i.e., the relative proximity of another dwarf galaxy.

Specifically, for each interacting dwarf galaxy, we selected three dwarf galaxies within $\Delta z=0.05$ and $\Delta \log(M_*/M_\odot)=0.3$, residing in the GOODS-South field, for which the same depth of X-ray observations can be achieved, without spectroscopically confirmed neighbors within 200 kpc. For each potential control sample dwarf, we also examined available archival imaging and excluded those dwarfs that are involved in an ongoing merger with uncataloged neighbors or dwarfs exhibiting clear tidal debris that might be due to ongoing or previous interaction ([Kado-Fong et al. 2020](#)). We started by selecting spectroscopically confirmed isolated dwarfs most similar to their interacting counterparts in terms of redshift and stellar mass. However, in some cases due to the combination of high- z and low stellar mass, we were unable to locate appropriate spectroscopically confirmed isolated dwarfs (e.g., lower-mass companions in id36, id70). In these cases, we included dwarfs with well-constrained photometric redshifts, i.e., those dwarfs with redshift uncertainties estimated at the 95% confidence limits meeting the criterion of $|z_{\text{upper/lower}} - z_{\text{phot}}| < 0.05$. These modest variations of redshift do not drastically affect the stellar mass estimates nor the presumed isolation of control sample dwarfs. We find, in total, 183 unique isolated control sample dwarfs, three for each of the 61 interacting dwarfs. A comparison between interacting and iso-

lated control sample dwarfs is shown in Figure 4, where it can be seen that they follow the same distribution in the stellar mass-redshift space.

We then performed an identical search for AGN in the isolated control sample. We crossmatched the control sample dwarfs with the Chandra Source Catalog, looking for X-ray sources within $1''$ of each dwarf, and we found three matches implying AGN frequency of $1.6\%_{-0.8}^{+1.6}$. Various other works examined the AGN occupation fractions in dwarf galaxies using multiwavelength approaches. For example, Reines et al. (2013) found a 0.5% occupation fraction at optical wavelengths. This value likely underestimates the true occupation fraction because of the combination of selection biases and limitations of existing optical diagnostics methods. The sample of dwarf galaxies was derived from a shallow SDSS survey, which, except for the nearest dwarfs, favors more luminous dwarfs. The enhanced luminosity usually signals a prevalent younger stellar population and ongoing star formation. Active star formation tends to overpower the optical signatures of AGN, thus rendering the optical BPT diagnostics methods (Baldwin et al. 1981) inaccurate for these types of works. On the other hand, Kaviraj et al. (2019) used infrared observations to find that AGN occupation fraction in dwarf galaxies can vary from 10% to 30%. Lupi et al. (2020) reanalyzed this work, taking into account the poor angular resolution of the infrared observations and the well-known fact that star formation processes can mimic typical AGN signatures in dwarf galaxies (Hainline et al. 2016), and found an occupation fraction of only 0.4%. Some recent works suggest that dwarf galaxies indeed have significantly higher AGN fractions. Mezcua & Sánchez (2024) studied dwarf galaxies from the MaNGA survey using a spaxel-by-spaxel classification in three spatially-resolved emission line diagnostic diagrams. This approach resulted in an AGN fraction of 20%, indicating that integral field spectroscopy is a powerful tool to reveal previously unknown faint and low-accreting dwarf AGN. Dickey et al. (2019) performed long-slit spectroscopy of 20 isolated, quenched dwarf galaxies, where star-formation pollution is expected to be minimal, and found a remarkable 80% AGN fraction. Pacucci et al. (2021) developed a theoretical model that utilizes the physical properties of galaxies, such as stellar mass and angular momentum, to predict multiwavelength AGN fractions of 5%-30%, increasing with increased stellar mass and decreased metallicity.

The apparent ambiguity of dwarf AGN fractions in existing literature is not unexpected. The use of different wavelengths and approaches will achieve different AGN luminosity depths and thus probe different AGN

populations. In order to properly evaluate the validity of our control sample AGN fraction, we must focus on X-ray studies probing comparable AGN luminosity levels. Latimer et al. (2021) used the eROSITA telescope, at X-ray wavelengths, to find an upper limit on dwarf galaxy AGN incidence of 1.8%. Mezcua et al. (2018) studied dwarfs from the Chandra COSMOS Legacy Survey and found occupation fraction of $\sim 0.4\%$ at $z < 0.4$ and $L_X > 10^{41}$ erg s^{-1} . Similarly, Pardo et al. (2016) used Chandra to find dwarf AGN fractions of 0.6%-3% at $z < 0.6$ and $L_X > 10^{41}$ erg s^{-1} . Finally, Birchall et al. (2020) studied SDSS dwarf galaxies at X-ray wavelengths with XMM-Newton and found AGN incidence to be between $\sim 0.5\%$ in the least massive stellar-mass bin, up to $\sim 1\%$ in the most massive stellar-mass bin calculated at $L_X > 3 \times 10^{40}$. When a lower limit of $L_X > 10^{39}$ is considered, the AGN fraction increases from 2.5% to 5.5% in the lowest and highest mass bins, respectively. If detection limits are further reduced, the AGN fraction would likely grow. However, reaching extremely low X-ray luminosity detection limits for a large sample of dwarfs would be observationally expensive. Furthermore, such very low-luminosity AGN would be almost impossible to distinguish from stellar-mass X-ray emitters with current technical capabilities. This review of the literature suggests that even though certain approaches yield large dwarf AGN fractions due to their superior sensitivity, the X-ray-based works consistently find low AGN fractions, in accordance with the AGN fraction we found in our control sample.

Therefore, the AGN frequency we found in the interacting sample indicates enhanced AGN presence by a factor of six up to a factor of ten, depending on the limit observed. The statistical significance of our discovery is from $\sim 4.3\sigma$ in the lower limit of the number of interacting AGN, up to $\sim 6.7\sigma$ in the AGN upper limit scenario. We conclude that dwarf-dwarf galaxy interactions play a significant role in triggering activity and subsequent growth of black holes. A comparison between AGN frequency we found in interacting dwarf galaxies and isolated control sample dwarf galaxies, and various X-ray-based works from the literature is shown in Figure 5.

4. CONCLUSIONS

The idea that galaxy interactions trigger AGN in dwarfs is not novel. Different simulations studied minor mergers involving galaxies with disproportional masses where one galaxy could be a dwarf. It was found that the secondary AGN can react dramatically to the interaction and undergo brief but violent episodes of accretion that can increase the mass of the black hole

by ten times, representing a viable channel for rapid black hole growth (Pfeifle et al. 2023, and references therein). Some recent observational works managed to detect mergers of dwarfs and their more massive companions with secondary AGN dominating the primary, suggesting ongoing intensive accretion processes (Secrest et al. 2017; Mićić et al. 2024). However, in the cosmological context, dwarf-dwarf mergers play an integral role in understanding the early evolutionary paths of supermassive black holes. Even though conditions in the early Universe remain beyond our reach, the prevailing wisdom is that concurrent and consecutive mergers involving dwarf galaxies are a common

sight. In this paper, we presented a new sample of dwarf galaxy systems, the first sample of dwarf-dwarf-merger-related AGN, and unambiguous evidence that dwarf-dwarf mergers are efficient in triggering black hole accretion. These findings are, for the first time, opening a window for future studies of mechanisms that dictate the earliest stages of growth of supermassive black holes.

The authors thank the anonymous referee for providing insightful comments that greatly improved the manuscript.

Table 1. Summary of spectroscopically confirmed dwarf-dwarf pairs

ID	RA	Dec	Field	z	z source	$\log M_*$	r_{sep}	M_{1^*}/M_{2^*}
	(deg)	(deg)				(M_{\odot})	(kpc)	
(1)	(2)	(3)	(4)	(5)	(6)	(7)	(8)	(9)
id1	189.04290771	62.19090271	GOODS-N	0.7728	s	9.41		
	189.04084778	62.19153976	GOODS-N	0.7732	s	9.14	31	1.9:1
id2	53.2062912	-27.85160446	GOODS-S	0.7836	s	9.53		
	53.20492554	-27.85132599	GOODS-S	0.7838	s	8.88	34	4.5:1
id3	53.07991409	-27.74620056	GOODS-S	0.2180	s	8.69		
	53.08021927	-27.74412537	GOODS-S	0.2170	s	8.44	27	1.8:1
id4	189.37626648	62.32131577	GOODS-N	0.8357	s	9.34		
	189.37515259	62.32249832	GOODS-N	0.8360	s	9.15	36	1.5:1
id5	189.151474	62.27391815	GOODS-N	0.8520	s	9.68		
	189.15444946	62.27086258	GOODS-N	0.8518	s	9.36	94	2.1:1
id6	189.16722107	62.2768631	GOODS-N	0.8490	s	9.66		
	189.1685791	62.27826691	GOODS-N	0.8486	s	9.00	43	4.6:1
id7	53.09305954	-27.89606667	GOODS-S	0.9666	s	9.69		
	53.09386063	-27.8982563	GOODS-S	0.9670	s	9.64	67	1.1:1
id8	53.21165085	-27.89239502	GOODS-S	0.9860	s	9.21		
	53.21179199	-27.89239502	GOODS-S	0.9860	s	9.06	4	1.4:1
id9	189.2885437	62.33514786	GOODS-N	1.0111	s	9.71		
	189.29125977	62.33637619	GOODS-N	1.0107	s	9.00	52	5.1:1
id10	53.06583786	-27.77513313	GOODS-S	1.0230	s	9.48		
	53.0657959	-27.77492905	GOODS-S	1.0230	s	9.33	6	1.4:1
id11	189.115448	62.16436386	GOODS-N	1.2146	s	9.57		
	189.11901855	62.16487122	GOODS-N	1.2160	s	9.02	53	3.5:1
id12	53.06857681	-27.78397751	GOODS-S	1.2187	s	9.55		
	53.06773376	-27.78424454	GOODS-S	1.2190	s	9.50	24	1.1:1
id13	189.11444092	62.17165375	GOODS-N	0.2532	s	9.07		

Table 1 *continued*

Table 1 (continued)

ID	RA	Dec	Field	z	z source	$\log M_*$	rsep	M_{1^*}/M_{2^*}
	(deg)	(deg)				(M_\odot)	(kpc)	
(1)	(2)	(3)	(4)	(5)	(6)	(7)	(8)	(9)
	189.11122131	62.17215729	GOODS-N	0.2540	s	7.92	23	14.1:1
id14	189.1065979	62.14515686	GOODS-N	1.2630	s	9.46		
	189.10676575	62.14500046	GOODS-N	1.2630	s	9.34	5	1.3:1
id15	53.15553665	-27.91340637	GOODS-S	1.3410	s	9.30		
	53.15535736	-27.91337013	GOODS-S	1.3410	s	8.59	5	5.1:1
id16	53.20502853	-27.74331856	GOODS-S	0.2164	s	9.26		
	53.20407486	-27.74143219	GOODS-S	0.2162	s	8.24	26	10.5:1
id17	214.79377747	52.81565857	AEGIS	0.2837	s	9.39		
	214.78594971	52.81204605	AEGIS	0.2837	s	8.38	93	10.2:1
id18	189.17329407	62.15087128	GOODS-N	0.2754	s	8.51		
	189.16664124	62.14615631	GOODS-N	0.2758	s	8.08	88	2.7:1
id19	189.25950623	62.17575836	GOODS-N	0.2762	s	7.72		
	189.25942993	62.17593384	GOODS-N	0.2760	s	7.40	3	2.1:1
id20	150.15498352	2.32654262	COSMOS	0.2831	s	9.53		
	150.15553284	2.32628226	COSMOS	0.2832	s	9.07	9	2.9:1
id21	53.0802536	-27.80839348	GOODS-S	0.2880	s	9.18		
	53.07812881	-27.8094635	GOODS-S	0.2870	s	8.76	34	2.6:1
id22	214.73500061	52.73179245	AEGIS	0.2909	s	9.43		
	214.73638916	52.73101807	AEGIS	0.2909	s	9.41	18	1:1
id23	214.82722473	52.82629013	AEGIS	0.2962	s	8.09		
	214.83213806	52.82337189	AEGIS	0.2962	s	8.08	67	1:1
id24	189.24482727	62.21456146	GOODS-N	0.3201	s	9.40		
	189.2419281	62.21679306	GOODS-N	0.3204	s	8.41	44	9.8:1
id25	53.22335434	-27.8624115	GOODS-S	0.3352	s	8.52		
	53.22351837	-27.86248207	GOODS-S	0.3352	s	7.61	3	8.1:1
id26	214.95265198	52.93842697	AEGIS	0.3134	s	9.67		
	214.95510864	52.93862915	AEGIS	0.3122	s	8.35	25	20.9:1
id27	214.72950745	52.7573967	AEGIS	0.4043	s	9.49		
	214.72917175	52.75977707	AEGIS	0.4042	s	8.77	47	5.2:1
id28	189.12519836	62.20683289	GOODS-N	0.4106	s	8.75		
	189.12475586	62.20670319	GOODS-N	0.4100	s	7.70	5	11.2:1
id29	53.16929245	-27.93000412	GOODS-S	0.1274	s	7.45		
	53.16825104	-27.93003845	GOODS-S	0.1270	s	7.24	8	1.6:1
id30	189.24327087	62.26353455	GOODS-N	0.4565	s	9.30		
	189.24397278	62.26481628	GOODS-N	0.4567	s	8.37	28	8.5:1
id31	189.38896179	62.23109055	GOODS-N	0.5105	s	9.50		
	189.38467407	62.22917175	GOODS-N	0.5101	s	8.66	62	6.9:1
id32	189.21343994	62.18349075	GOODS-N	0.5174	s	9.00		

Table 1 continued

Table 1 (continued)

ID	RA	Dec	Field	z	z source	$\log M_*$	rsep	M_{1^*}/M_{2^*}
	(deg)	(deg)				(M_\odot)	(kpc)	
(1)	(2)	(3)	(4)	(5)	(6)	(7)	(8)	(9)
	189.21533203	62.18114853	GOODS-N	0.5180	s	8.78	56	1.7:1
id33	34.37569809	-5.22611809	UDS	0.5340	s	9.36		
	34.37714386	-5.22825003	UDS	0.5340	s	9.27	59	1.2:1
id34	53.04432297	-27.78720093	GOODS-S	0.5781	s	8.93		
	53.04456711	-27.78714943	GOODS-S	0.5781	s	8.87	5	1.1:1
id35	189.26983643	62.27832413	GOODS-N	0.6041	s	9.03		
	189.2701416	62.27870178	GOODS-N	0.6041	s	8.83	10	1.6:1
id36	53.07033539	-27.71787071	GOODS-S	0.6442	s	8.71		
	53.07018661	-27.7177639	GOODS-S	0.6442	s	7.72	4	9.8:1
id37	150.08889771	2.3513546	COSMOS	0.6684	s	9.05		
	150.08886719	2.35152078	COSMOS	0.6684	s	8.51	4	3.5:1
id38	189.02261353	62.21254349	GOODS-N	0.6789	s	8.89		
	189.02279663	62.21220016	GOODS-N	0.6789	s	8.39	9	3.2:1
id39	189.35325623	62.26233292	GOODS-N	0.6912	s	9.61		
	189.35220337	62.26305389	GOODS-N	0.6912	s	9.58	23	1.1:1
id40	214.97157288	52.93635559	AEGIS	0.7164	s	9.58		
	214.96983337	52.93461227	AEGIS	0.7162	s	8.92	53	4.6:1
id41	215.00022888	52.96072006	AEGIS	0.7439	s	9.06		
	214.99899292	52.96024323	AEGIS	0.7437	s	8.98	24	1.2:1
id42	214.76210022	52.77083588	AEGIS	0.7380	s	9.20		
	214.76611328	52.7721405	AEGIS	0.7379	s	8.85	73	2.2:1
id43	53.12589645	-27.75127602	GOODS-S	0.7380	s	9.55		
	53.12376785	-27.75199509	GOODS-S	0.7370	s	9.40	54	1.4:1
id44	214.78341675	52.84712601	AEGIS	0.7567	s	9.72		
	214.78218079	52.84781647	AEGIS	0.7568	s	8.44	27	19.1:1
id45	189.26382446	62.27958679	GOODS-N	0.7439	s	9.32		
	189.26036072	62.2792244	GOODS-N	0.7441	s	8.79	44	3.4:1
id46	189.28974915	62.19259644	GOODS-N	0.9064	s	9.73		
	189.28616333	62.19122696	GOODS-N	0.9072	s	9.48	62	1.8:1
id47	189.03062439	62.16661072	GOODS-N	0.9229	s	9.16		
	189.0272522	62.16641998	GOODS-N	0.9223	s	8.91	45	1.8:1
id48	53.14984894	-27.85508728	GOODS-S	0.3592	s	9.67		
	53.15156555	-27.8548851	GOODS-S	0.3588	s	9.48	28	1.5:1
id49	189.12135315	62.19810867	GOODS-N	0.5293	s	9.00		
	189.12417603	62.19818878	GOODS-N	0.5285	s	8.62	30	2.4:1
id50	214.89303589	52.7860527	AEGIS	0.6518	s	9.49		
	214.89216614	52.78372574	AEGIS	0.6528	s	9.17	60	2.1:1
id51	150.14634705	2.26014423	COSMOS	0.3725	s	9.53		

Table 1 continued

Table 1 (*continued*)

ID	RA	Dec	Field	z	z source	$\log M_*$	rsep	M_{1^*}/M_{2^*}
	(deg)	(deg)				(M_\odot)	(kpc)	
(1)	(2)	(3)	(4)	(5)	(6)	(7)	(8)	(9)
	150.14990234	2.2571671	COSMOS	0.3715	s	8.81	87	5.2:1

NOTE—(1) System ID; (2) Right ascension; (3) Declination; (4) Field name; (5) Redshift; (6) Source of redshift (s-spectroscopic, p-photometric). For photometric redshifts 95% confidence limits are reported from Momcheva et al. (2016); (7) Stellar mass in $\log(M_*/M_\odot)$; (8) Projected separation in kpc between the most massive dwarf and its neighbor(s); (9) Mass ratios between the most massive dwarf and its neighbor(s).

Table 2. Summary of spectroscopically confirmed dwarf groups

ID	RA	Dec	Field	z	z source	$\log M_*$	rsep	M_{1^*}/M_{2^*}
	(deg)	(deg)				(M_\odot)	(kpc)	
(1)	(2)	(3)	(4)	(5)	(6)	(7)	(8)	(9)
id52	189.09373474	62.16689682	GOODS-N	0.7504	s	9.58		
	189.09140015	62.16662598	GOODS-N	0.7504	s	9.11	30	2.9:1
	189.09063721	62.16683197	GOODS-N	0.7504	s	8.76	39	6.6:1
id53	215.00132751	52.9636879	AEGIS	0.7444	s	9.56		
	215.00022888	52.96072006	AEGIS	0.7439	s	9.06	89	3.2:1
	214.99899292	52.96024323	AEGIS	0.7437	s	8.98	90	3.8:1
id54	189.32987976	62.25835037	GOODS-N	0.8419	s	9.39		
	189.33276367	62.258979	GOODS-N	0.8421	s	9.25	32	1.4:1
	189.33218384	62.2587204	GOODS-N	0.8423	s	8.90	41	3.1:1
id55	189.24627686	62.31162643	GOODS-N	1.0110	s	9.59		
	189.24359131	62.31165314	GOODS-N	1.0111	s	9.56	37	1.1:1
	189.24624634	62.31002808	GOODS-N	1.0120	s	9.11	47	3:1
id56	189.12358093	62.20001221	GOODS-N	1.0153	s	9.39		
	189.1244812	62.2002449	GOODS-N	1.0160	s	9.00	14	2.4:1
	189.12409973	62.20019531	GOODS-N	1.0160	s	8.80	9	3.1:1
id57	214.98876953	52.85660934	AEGIS	0.3340	s	9.14		
	214.98529053	52.85574341	AEGIS	0.3342	s	9.00	39	1.4:1
	214.98249817	52.85441971	AEGIS	0.3335	s	8.43	76	5.1:1
id58	189.31768799	62.22966385	GOODS-N	0.4475	s	9.73		
	189.31654358	62.23021317	GOODS-N	0.4466	s	8.58	16	14.1:1
	189.31764221	62.23020554	GOODS-N	0.4465	s	8.52	11	16.2:1
id59	189.40246582	62.33492661	GOODS-N	0.5857	s	9.40		
	189.40385437	62.33591843	GOODS-N	0.5856	s	9.11	28	1.9:1
	189.39904785	62.33481979	GOODS-N	0.5857	s	9.07	38	2.1:1

Table 2 *continued*

Table 2 (*continued*)

ID	RA	Dec	Field	z	z source	$\log M_*$	rsep	M_{1^*}/M_{2^*}
	(deg)	(deg)				(M_\odot)	(kpc)	
(1)	(2)	(3)	(4)	(5)	(6)	(7)	(8)	(9)
	189.40063477	62.33504105	GOODS-N	$0.5656^{+0.1204}_{-0.1366}$	p	7.98	21	26.3:1

NOTE—(1) System ID; (2) Right ascension; (3) Declination; (4) Field name; (5) Redshift; (6) Source of redshift (s-spectroscopic, p-photometric). For photometric redshifts 95% confidence limits are reported from [Momcheva et al. \(2016\)](#); (7) Stellar mass in $\log(M_*/M_\odot)$; (8) Projected separation in kpc between the most massive dwarf and its neighbor(s); (9) Mass ratios between the most massive dwarf and its neighbor(s).

Table 3. Summary of candidates for dwarf-dwarf pairs and groups

ID	RA	Dec	Field	z	z source	$\log M_*$	rsep	M_{1^*}/M_{2^*}
	(deg)	(deg)				(M_\odot)	(kpc)	
(1)	(2)	(3)	(4)	(5)	(6)	(7)	(8)	(9)
id60	189.22039795	62.28197098	GOODS-N	0.7614	s	8.77		
	189.22059631	62.28224182	GOODS-N	$0.7610^{+0.1010}_{-0.0730}$	p	8.54	8	1.7:1
id61	150.11117554	2.25387931	COSMOS	0.7767	s	9.61		
	150.11143494	2.25390387	COSMOS	$0.7771^{+0.0024}_{-0.0030}$	p	8.84	7	5.9:1
id62	189.17056274	62.27451324	GOODS-N	0.7802	s	9.71		
	189.16990662	62.27450562	GOODS-N	$0.7816^{+0.0034}_{-0.0053}$	p	9.41	8	2:1
id63	189.17514038	62.22260284	GOODS-N	0.8460	s	9.15		
	189.17657471	62.22203827	GOODS-N	$0.8487^{+0.0040}_{-0.0027}$	p	9.03	24	1.3:1
id64	189.32949829	62.35944748	GOODS-N	0.9458	s	9.43		
	189.32531738	62.35821152	GOODS-N	$0.9455^{+0.0046}_{-0.0043}$	p	9.24	66	1.5:1
id65	53.13801193	-27.69859123	GOODS-S	$0.9523^{+0.0019}_{-0.0038}$	p	9.46		
	53.13689041	-27.69883156	GOODS-S	0.9510	s	9.18	29	1.9:1
id66	214.8289032	52.83329773	AEGIS	$0.9582^{+0.0024}_{-0.0030}$	p	9.34		
	214.82546997	52.83427429	AEGIS	0.9600	s	9.27	66	1.2:1
id67	53.17535019	-27.85260391	GOODS-S	0.9616	s	9.39		
	53.17354202	-27.85242081	GOODS-S	$0.9630^{+0.0029}_{-0.0126}$	p	9.15	47	1.7:1
id68	53.07076645	-27.85066795	GOODS-S	0.9900	s	9.59		
	53.0722084	-27.84975815	GOODS-S	$0.9917^{+0.0182}_{-0.0099}$	p	9.12	45	2.9:1
id69	214.92391968	52.82198715	AEGIS	0.8390	s	9.03		
	214.92401123	52.82240295	AEGIS	$0.8368^{+0.0043}_{-0.0042}$	p	8.68	12	2.2:1
id70	189.27220154	62.17921829	GOODS-N	1.0230	s	9.46		
	189.27285767	62.17891693	GOODS-N	$1.0262^{+0.1128}_{-0.1592}$	p	8.28	13	15.1:1
id71	189.14463806	62.16677856	GOODS-N	$1.2111^{+0.0082}_{-0.0175}$	p	9.18		
	189.14497375	62.16666412	GOODS-N	1.2174	s	9.14	8	1.1:1

Table 3 *continued*

Table 3 (continued)

ID	RA	Dec	Field	z	z source	$\log M_*$	rsep	M_{1^*}/M_{2^*}
	(deg)	(deg)				(M_\odot)	(kpc)	
(1)	(2)	(3)	(4)	(5)	(6)	(7)	(8)	(9)
id72	53.08846283	-27.76522827	GOODS-S	1.2240	s	9.22		
	53.08879471	-27.76517105	GOODS-S	$1.2233^{+0.0016}_{-0.0038}$	p	8.87	9	2.2:1
id73	53.16807938	-27.72351074	GOODS-S	1.2434	s	9.59		
	53.16835785	-27.72373772	GOODS-S	$1.2453^{+0.0857}_{-0.1013}$	p	9.02	10	3.7:1
id74	53.11321259	-27.83273125	GOODS-S	1.2930	s	9.64		
	53.11421585	-27.83185387	GOODS-S	$1.2945^{+0.0022}_{-0.0033}$	p	9.10	38	3.5:1
id75	189.13853455	62.23644638	GOODS-N	1.3448	s	9.52		
	189.13601685	62.23694611	GOODS-N	$1.3486^{+0.1054}_{-0.1206}$	p	9.02	39	3.2:1
id76	189.10520935	62.18302917	GOODS-N	1.3500	s	9.55		
	189.10534668	62.18320084	GOODS-N	$1.3446^{+0.0914}_{-0.1036}$	p	9.04	6	3.2:1
id77	53.10016632	-27.84272003	GOODS-S	1.4130	s	9.71		
	53.09990311	-27.84256554	GOODS-S	$1.4177^{+0.2593}_{-0.1167}$	p	8.81	9	7.9:1
id78	189.16906738	62.23484421	GOODS-N	$1.4805^{+0.2225}_{-0.1405}$	p	9.28		
	189.16880798	62.23432541	GOODS-N	1.4856	s	9.13	17	1.4:1
id79	189.30671692	62.33421707	GOODS-N	0.2777	s	8.61		
	189.30674744	62.33452988	GOODS-N	$0.2770^{+0.0054}_{-0.0056}$	p	7.89	5	5.2:1
id80	189.29902649	62.25413895	GOODS-N	0.2990	s	9.56		
	189.30000305	62.25340652	GOODS-N	$0.3028^{+0.0328}_{-0.0477}$	p	8.19	14	23.4:1
id81	53.16155624	-27.79225731	GOODS-S	0.4580	s	9.11		
	53.16196442	-27.79255295	GOODS-S	$0.4528^{+0.0315}_{-0.0106}$	p	8.79	10	2.1:1
id82	53.22396469	-27.81417465	GOODS-S	0.1483	s	8.16		
	53.22394943	-27.81487083	GOODS-S	$0.1434^{+0.0389}_{-0.0188}$	p	7.63	6	3.4:1
id83	150.08700562	2.3090229	COSMOS	0.6875	s	9.19		
	150.08738708	2.3089335	COSMOS	$0.6846^{+0.0049}_{-0.0080}$	p	8.87	10	2.1:1
id84	53.09656143	-27.92811012	GOODS-S	0.7334	s	9.50		
	53.09663391	-27.92639351	GOODS-S	$0.7350^{+0.0077}_{-0.0061}$	p	8.79	46	5.1:1
id85	214.75852966	52.75759506	AEGIS	0.8456	s	9.63		
	214.75782776	52.75798035	AEGIS	$0.8404^{+0.0024}_{-0.0034}$	p	9.05	16	3.8:1
id86	53.15167999	-27.77537727	GOODS-S	$1.0391^{+0.0061}_{-0.0189}$	p	9.71		
	53.15179062	-27.77550697	GOODS-S	1.0470	s	9.09	5	4.2:1
id87	150.06022644	2.28915334	COSMOS	0.6041	s	9.38		
	150.06088257	2.28896928	COSMOS	$0.5968^{+0.0390}_{-0.0203}$	p	9.03	17	2.2:1
id88	214.88000488	52.87176514	AEGIS	0.6913	s	9.13		
	214.8795929	52.87166214	AEGIS	$0.6930^{+0.1076}_{-0.0192}$	p	8.77	7	2.3:1
id89	214.96824646	52.91167831	AEGIS	0.7684	s	9.31		
	214.96798706	52.9119873	AEGIS	$0.7674^{+0.0578}_{-0.0096}$	p	8.91	9	2.5:1
id90	189.3994751	62.24066925	GOODS-N	1.1403	s	9.70		
	189.39570618	62.23989487	GOODS-N	$1.1436^{+0.0431}_{-0.0926}$	p	9.44	58	1.8:1

Table 3 continued

Table 3 (*continued*)

ID	RA	Dec	Field	z	z source	$\log M_*$	rsep	M_{1^*}/M_{2^*}
	(deg)	(deg)				(M_\odot)	(kpc)	
(1)	(2)	(3)	(4)	(5)	(6)	(7)	(8)	(9)
id91	53.14494324	-27.84020996	GOODS-S	0.9778	s	9.42		
	53.1451683	-27.84038353	GOODS-S	$0.9818^{+0.0032}_{-0.0029}$	p	9.42	8	1:1
	53.14426041	-27.84013176	GOODS-S	$0.9807^{+0.0553}_{-0.0717}$	p	8.89	18	3.4:1
id92	53.18664551	-27.83599281	GOODS-S	1.2960	s	9.59		
	53.18647766	-27.83611488	GOODS-S	1.2960	s	9.31	6	1.9:1
	53.18729401	-27.83481789	GOODS-S	$1.3002^{+0.0022}_{-0.0034}$	p	9.52	40	1.2;1
id93	53.19279099	-27.91669655	GOODS-S	$1.4330^{+0.0730}_{-0.0700}$	p	9.52		
	53.19335938	-27.91612625	GOODS-S	$1.4242^{+0.0021}_{-0.0032}$	p	9.00	23	3.3:1
	53.19394302	-27.91622162	GOODS-S	1.4250	s	9.12	34	2.5:1

NOTE—(1) System ID; (2) Right ascension; (3) Declination; (4) Field name; (5) Redshift; (6) Source of redshift (s-spectroscopic, p-photometric). For photometric redshifts 95% confidence limits are reported from [Momcheva et al. \(2016\)](#); (7) Stellar mass in $\log(M_*/M_\odot)$; (8) Projected separation in kpc between the most massive dwarf and its neighbor(s); (9) Mass ratios between the most massive dwarf and its neighbor(s).

Table 4. Summary of X-ray detected AGN

ID	RA	Dec	$\log L_X$	$\log M_*$	$\log \text{SFR}$	$\log L_{XRB}$	$\log L_{hot}$	$\log L_{AGN}$
	(deg)	(deg)	(erg s^{-1})	(M_\odot)	($M_\odot \text{ yr}^{-1}$)	(erg s^{-1})	(erg s^{-1})	(erg s^{-1})
(1)	(2)	(3)	(4)	(5)	(6)	(7)	(8)	(9)
id3	53.0798	-27.7462	40.18	8.69	0.18	39.40 ± 0.07	39.09 ± 0.01	40.06 ± 0.02
id10	53.0658	-27.7750	41.54	9.33	1.17	40.38 ± 0.06	39.98 ± 0.01	41.50 ± 0.02
id34	53.0444	-27.7875	41.21	8.93	-0.10	39.13 ± 0.06	38.7 ± 0.01	41.20 ± 0.01
id43	53.1259	-27.7514	43.56	9.55	1.22	40.43 ± 0.06	40.04 ± 0.01	43.56 ± 0.00
id86	53.1518	-27.7755	41.74	9.09	1.35	40.56 ± 0.06	40.17 ± 0.01	41.70 ± 0.00
id91	53.1450	-27.8403	41.96	9.42	1.01	40.22 ± 0.06	39.83 ± 0.01	41.86 ± 0.00

NOTE—(1) Corresponding system ID; (2) X-ray source right ascension; (3) X-ray source declination; (4) K-corrected X-ray luminosity calculated adopting the redshift of the host galaxy as distance and using the aperture-corrected net energy flux from the point spread function 90% enclosed-count fraction aperture in the rest-frame 0.5-10 keV in units $\text{erg s}^{-1} \text{ cm}^{-2}$. For id3, id10, id34, id43, and id91 reported X-ray flux is derived from the longest observation; for id87 reported X-ray flux is derived by averaging over all contributing observations; (5) Stellar mass of the host galaxy (6) Star formation rate of the host galaxy adopted from [Momcheva et al. \(2016\)](#) (7) X-ray binary contribution to the observed X-ray flux calculated using [Lehmer et al. \(2010\)](#); (8) Hot interstellar medium contribution to the observed X-ray flux calculated using [Mineo et al. \(2012\)](#) (9) Corrected AGN X-ray luminosity.

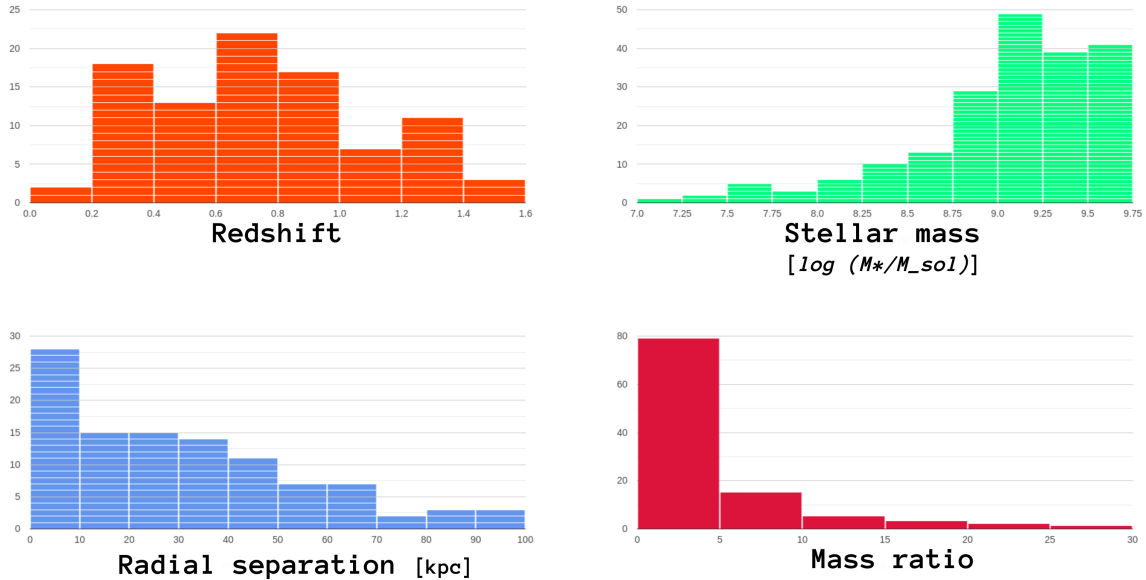


Figure 1. Demographics of paired/grouped dwarfs. Upper left: Redshift distribution of paired/grouped dwarf systems. Upper right: Stellar mass distribution of all dwarfs from paired/grouped dwarf systems. Lower left: Distribution of projected separation between the most massive dwarf and their neighbor(s). Lower right: Distribution of the mass ratios of the most massive dwarf and their neighbor(s).

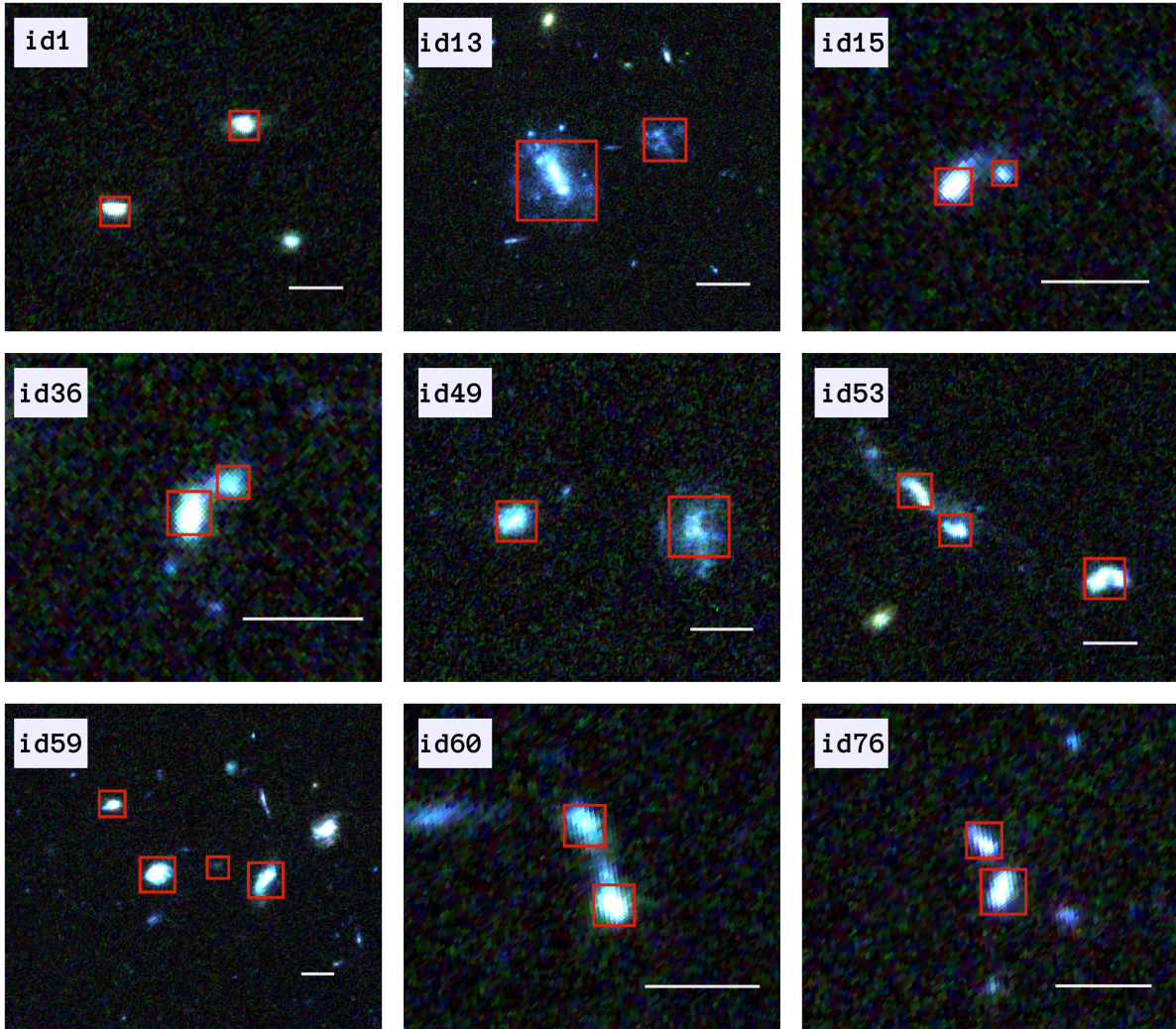


Figure 2. GOODS color images of nine randomly selected dwarf systems. The identification number of each system is given in the upper left corner. The white horizontal lines in the lower right corner represent ≈ 10 kpc. The galaxies of interest are labeled with red rectangles.

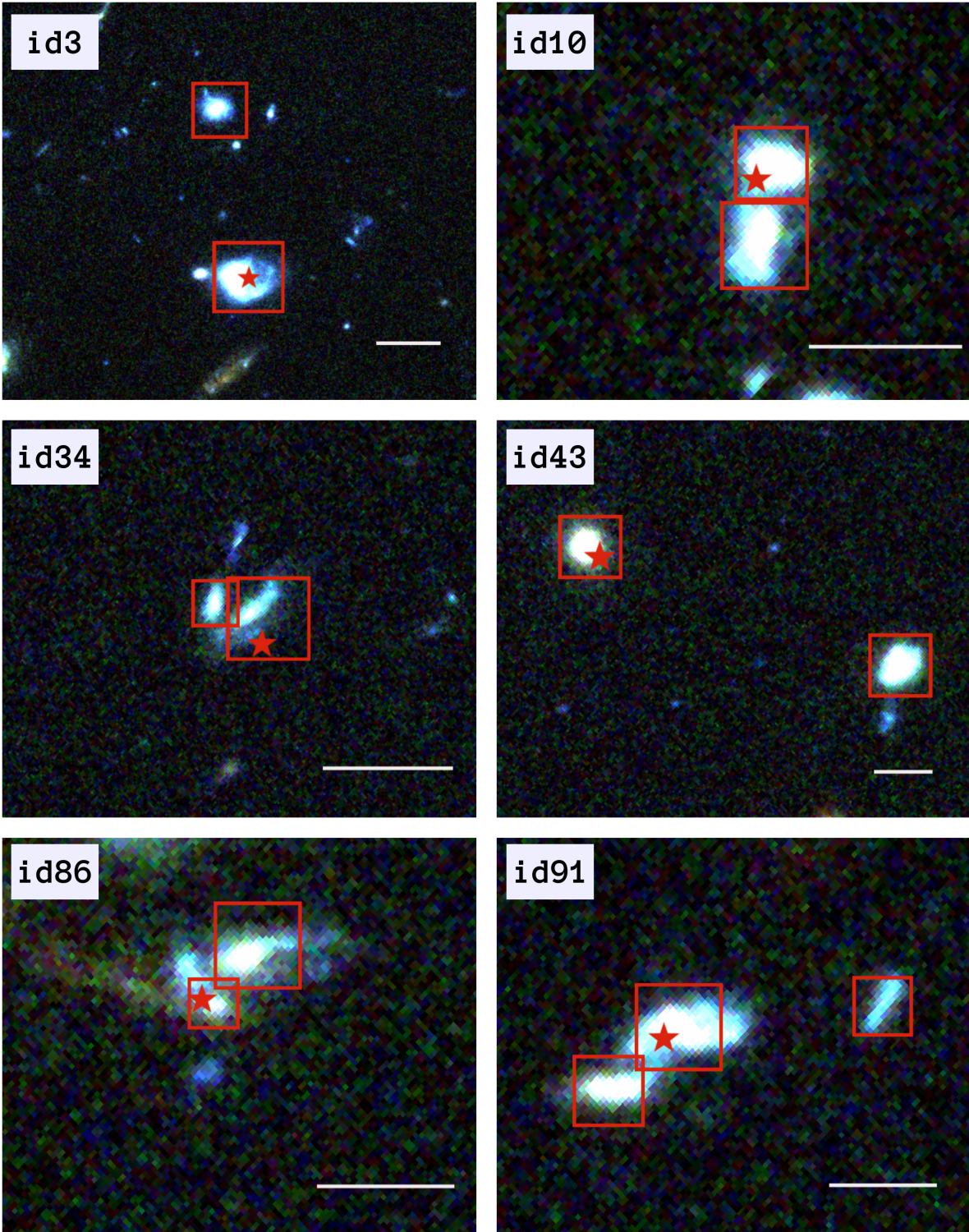


Figure 3. GOODS color images of the six dwarf pairs/groups hosting an AGN. The identification number of each system is given in the upper left corner. Horizontal white lines in the lower right corner represent ≈ 10 kpc. Galaxies of interest are located in red rectangles. Red star symbols represent the location of Chandra X-ray detected AGN.

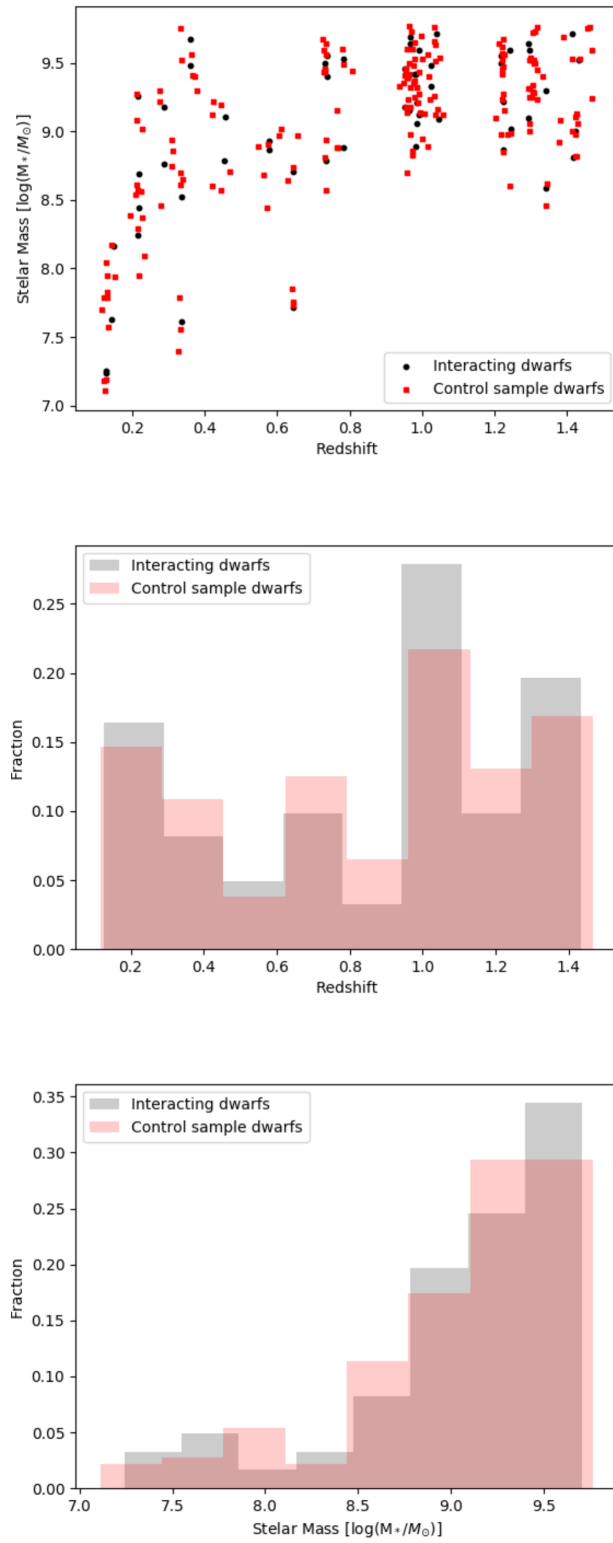


Figure 4. Top: Distribution of interacting and isolated control dwarf galaxies in redshift-stellar mass space. Middle: Redshift distribution of interacting and isolated control dwarf galaxies. Bottom: Stellar mass distribution of interacting and isolated control dwarf galaxies.

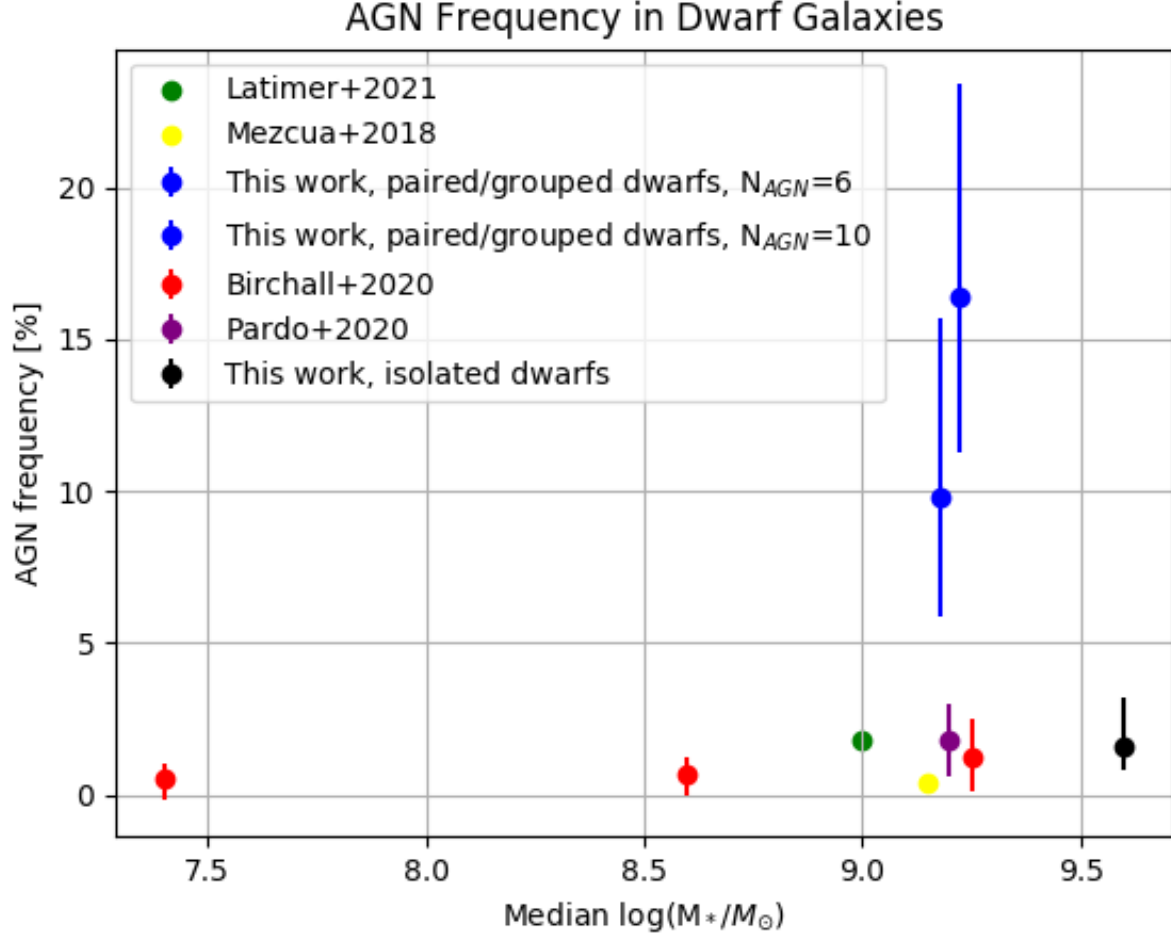


Figure 5. AGN frequency in paired/grouped dwarfs in both $N_{AGN,low}=6$ and $N_{AGN,high}=10$ limits compared to the occupation fraction in isolated control sample and occupation fraction from the literature as a function of the median stellar mass of dwarfs hosting an AGN. Uncertainties from our work are estimated at 1σ assuming Poissonian statistics. Latimer et al. (2021) does not provide the list of galaxies in their sample, thus the median stellar mass of the sample is set to $\log(M_*/M_\odot)=9.0$.

REFERENCES

- Atek, H., Labbé, I., Furtak, L. J., et al. 2024, *Nature*, 626, 975, doi: [10.1038/s41586-024-07043-6](https://doi.org/10.1038/s41586-024-07043-6)
- Baldwin, J. A., Phillips, M. M., & Terlevich, R. 1981, *PASP*, 93, 5, doi: [10.1086/130766](https://doi.org/10.1086/130766)
- Bañados, E., Venemans, B. P., Mazzucchelli, C., et al. 2018, *Nature*, 553, 473, doi: [10.1038/nature25180](https://doi.org/10.1038/nature25180)
- Barrows, R. S., Comerford, J. M., Greene, J. E., & Pooley, D. 2017, *The Astrophysical Journal*, 838, 129, doi: [10.3847/1538-4357/aa64d9](https://doi.org/10.3847/1538-4357/aa64d9)
- Birchall, K. L., Watson, M. G., & Aird, J. 2020, *Monthly Notices of the Royal Astronomical Society*, 492, 2268, doi: [10.1093/mnras/staa040](https://doi.org/10.1093/mnras/staa040)
- Bogdán, Á., Goulding, A. D., Natarajan, P., et al. 2024, *Nature Astronomy*, 8, 126, doi: [10.1038/s41550-023-02111-9](https://doi.org/10.1038/s41550-023-02111-9)
- Bromm, V., & Loeb, A. 2003, *The Astrophysical Journal*, 596, 34, doi: [10.1086/377529](https://doi.org/10.1086/377529)
- Bruzual, G., & Charlot, S. 2003, *Monthly Notices of the Royal Astronomical Society*, 344, 1000, doi: [10.1046/j.1365-8711.2003.06897.x](https://doi.org/10.1046/j.1365-8711.2003.06897.x)
- Chabrier, G. 2003, *The Publications of the Astronomical Society of the Pacific*, 115, 763, doi: [10.1086/376392](https://doi.org/10.1086/376392)
- Dickey, C. M., Geha, M., Wetzel, A., & El-Badry, K. 2019, *The Astrophysical Journal*, 884, 180, doi: [10.3847/1538-4357/ab3220](https://doi.org/10.3847/1538-4357/ab3220)
- Evans, I. N., Primini, F. A., Glotfelty, K. J., et al. 2010, *The Astrophysical Journal Supplement Series*, 189, 37, doi: [10.1088/0067-0049/189/1/37](https://doi.org/10.1088/0067-0049/189/1/37)
- Foord, A., Gültekin, K., Reynolds, M. T., et al. 2019, *The Astrophysical Journal*, 877, 17, doi: [10.3847/1538-4357/ab18a3](https://doi.org/10.3847/1538-4357/ab18a3)
- Fragos, T., Lehmer, B. D., Naoz, S., Zezas, A., & Basu-Zych, A. 2013, *The Astrophysical Journal Letters*, 776, L31, doi: [10.1088/2041-8205/776/2/L31](https://doi.org/10.1088/2041-8205/776/2/L31)
- Gao, F., Wang, L., Pearson, W. J., et al. 2020, *Astronomy & Astrophysics*, 637, A94, doi: [10.1051/0004-6361/201937178](https://doi.org/10.1051/0004-6361/201937178)
- Gehrels, N. 1986, *The Astrophysical Journal*, 303, 336, doi: [10.1086/164079](https://doi.org/10.1086/164079)
- Hainline, K. N., Reines, A. E., Greene, J. E., & Stern, D. 2016, *The Astrophysical Journal*, 832, 119, doi: [10.3847/0004-637X/832/2/119](https://doi.org/10.3847/0004-637X/832/2/119)
- Hickox, R. C., & Markevitch, M. 2006, *The Astrophysical Journal*, 645, 95, doi: [10.1086/504070](https://doi.org/10.1086/504070)
- Hopkins, P. F., & Hernquist, L. 2009, *The Astrophysical Journal*, 698, 1550, doi: [10.1088/0004-637X/698/2/1550](https://doi.org/10.1088/0004-637X/698/2/1550)
- Hopkins, P. F., Hernquist, L., Cox, T. J., & Kereš, D. 2008, *The Astrophysical Journal Supplement Series*, 175, 356, doi: [10.1086/524362](https://doi.org/10.1086/524362)
- Kado-Fong, E., Greene, J. E., Greco, J. P., et al. 2020, *AJ*, 159, 103, doi: [10.3847/1538-3881/ab6ef3](https://doi.org/10.3847/1538-3881/ab6ef3)
- Kaviraj, S., Martin, G., & Silk, J. 2019, *Monthly Notices of the Royal Astronomical Society: Letters*, 489, L12, doi: [10.1093/mnrasl/slz102](https://doi.org/10.1093/mnrasl/slz102)
- Kimbro, E., Reines, A. E., Molina, M., Deller, A. T., & Stern, D. 2021, *The Astrophysical Journal*, 912, 89, doi: [10.3847/1538-4357/abec6a](https://doi.org/10.3847/1538-4357/abec6a)
- Koss, M., Mushotzky, R., Treister, E., et al. 2012, *The Astrophysical Journal Letters*, 746, L22, doi: [10.1088/2041-8205/746/2/L22](https://doi.org/10.1088/2041-8205/746/2/L22)
- Latimer, L. J., Reines, A. E., Bogdan, A., & Kraft, R. 2021, *The Astrophysical Journal Letters*, 922, L40, doi: [10.3847/2041-8213/ac3af6](https://doi.org/10.3847/2041-8213/ac3af6)
- Lehmer, B. D., Alexander, D. M., Bauer, F. E., et al. 2010, *The Astrophysical Journal*, 724, 559, doi: [10.1088/0004-637X/724/1/559](https://doi.org/10.1088/0004-637X/724/1/559)
- Lehmer, B. D., Eufrazio, R. T., Basu-Zych, A., et al. 2022, *The Astrophysical Journal*, 930, 135, doi: [10.3847/1538-4357/ac63a7](https://doi.org/10.3847/1538-4357/ac63a7)
- Lehmer, B. D., Basu-Zych, A. R., Mineo, S., et al. 2016, *The Astrophysical Journal*, 825, 7, doi: [10.3847/0004-637X/825/1/7](https://doi.org/10.3847/0004-637X/825/1/7)
- Lemons, S. M., Reines, A. E., Plotkin, R. M., Gallo, E., & Greene, J. E. 2015, *The Astrophysical Journal*, 805, 12, doi: [10.1088/0004-637X/805/1/12](https://doi.org/10.1088/0004-637X/805/1/12)
- Li, W., Nair, P., Irwin, J., et al. 2023, *The Astrophysical Journal*, 944, 168, doi: [10.3847/1538-4357/acb13d](https://doi.org/10.3847/1538-4357/acb13d)
- Loeb, A., & Rasio, F. A. 1994, *The Astrophysical Journal*, 432, 52, doi: [10.1086/174548](https://doi.org/10.1086/174548)
- Lupi, A., Sbarrato, T., & Carniani, S. 2020, *Monthly Notices of the Royal Astronomical Society*, 492, 2528, doi: [10.1093/mnras/stz3636](https://doi.org/10.1093/mnras/stz3636)
- Madau, P., & Rees, M. J. 2001, *The Astrophysical Journal Letters*, 551, L27, doi: [10.1086/319848](https://doi.org/10.1086/319848)
- Mason, C. A., Trenti, M., & Treu, T. 2015, *The Astrophysical Journal*, 813, 21, doi: [10.1088/0004-637X/813/1/21](https://doi.org/10.1088/0004-637X/813/1/21)
- Mezcua, M., Civano, F., Fabbiano, G., Miyaji, T., & Marchesi, S. 2016, *The Astrophysical Journal*, 817, 20, doi: [10.3847/0004-637X/817/1/20](https://doi.org/10.3847/0004-637X/817/1/20)
- Mezcua, M., Civano, F., Marchesi, S., et al. 2018, *MNRAS*, 478, 2576, doi: [10.1093/mnras/sty1163](https://doi.org/10.1093/mnras/sty1163)
- Mezcua, M., & Sánchez, H. D. 2024, *Monthly Notices of the Royal Astronomical Society*, 528, 5252, doi: [10.1093/mnras/stae292](https://doi.org/10.1093/mnras/stae292)
- Mineo, S., Gilfanov, M., & Sunyaev, R. 2012, *Monthly Notices of the Royal Astronomical Society*, 426, 1870, doi: [10.1111/j.1365-2966.2012.21831.x](https://doi.org/10.1111/j.1365-2966.2012.21831.x)

- Mićić, M., Holmes, O. J., Wells, B. N., & Irwin, J. A. 2023, *The Astrophysical Journal*, 944, 160, doi: [10.3847/1538-4357/aca1bb](https://doi.org/10.3847/1538-4357/aca1bb)
- Mićić, M., Wells, B. N., Holmes, O. J., & Irwin, J. A. 2024, *The Open Journal of Astrophysics*, 7, doi: [10.21105/astro.2310.09945](https://doi.org/10.21105/astro.2310.09945)
- Momcheva, I. G., Brammer, G. B., van Dokkum, P. G., et al. 2016, *The Astrophysical Journal Supplement Series*, 225, 27, doi: [10.3847/0067-0049/225/2/27](https://doi.org/10.3847/0067-0049/225/2/27)
- Pacucci, F., Mezcuca, M., & Regan, J. A. 2021, *The Astrophysical Journal*, 920, 134, doi: [10.3847/1538-4357/ac1595](https://doi.org/10.3847/1538-4357/ac1595)
- Pardo, K., Goulding, A. D., Greene, J. E., et al. 2016, *The Astrophysical Journal*, 831, 203, doi: [10.3847/0004-637X/831/2/203](https://doi.org/10.3847/0004-637X/831/2/203)
- Paudel, S., Smith, R., Yoon, S. J., Calderón-Castillo, P., & Duc, P.-A. 2018, *The Astrophysical Journal Supplement Series*, 237, 36, doi: [10.3847/1538-4365/aad555](https://doi.org/10.3847/1538-4365/aad555)
- Pfeifle, R. W., Rothberg, B., Weaver, K. A., et al. 2023, *The Astrophysical Journal*, 945, 167, doi: [10.3847/1538-4357/acbd45](https://doi.org/10.3847/1538-4357/acbd45)
- Prieto, J., Escala, A., Privon, G. C., & d'Etigny, J. 2021, *Monthly Notices of the Royal Astronomical Society*, 508, 3672, doi: [10.1093/mnras/stab2740](https://doi.org/10.1093/mnras/stab2740)
- Reines, A. E., Greene, J. E., & Geha, M. 2013, *The Astrophysical Journal*, 775, 116, doi: [10.1088/0004-637X/775/2/116](https://doi.org/10.1088/0004-637X/775/2/116)
- Reines, A. E., Plotkin, R. M., Russell, T. D., et al. 2014, *The Astrophysical Journal Letters*, 787, L30, doi: [10.1088/2041-8205/787/2/L30](https://doi.org/10.1088/2041-8205/787/2/L30)
- Secrest, N. J., Schmitt, H. R., Blecha, L., Rothberg, B., & Fischer, J. 2017, *The Astrophysical Journal*, 836, 183, doi: [10.3847/1538-4357/836/2/183](https://doi.org/10.3847/1538-4357/836/2/183)
- Silva, A., Marchesini, D., Silverman, J. D., et al. 2021, *The Astrophysical Journal*, 909, 124, doi: [10.3847/1538-4357/abdbb1](https://doi.org/10.3847/1538-4357/abdbb1)
- Simmonds, C., Bauer, F. E., Thuan, T. X., et al. 2016, *Astronomy & Astrophysics*, 596, A64, doi: [10.1051/0004-6361/201629310](https://doi.org/10.1051/0004-6361/201629310)
- Skelton, R. E., Whitaker, K. E., Momcheva, I. G., et al. 2014, *The Astrophysical Journal Supplement Series*, 214, 24, doi: [10.1088/0067-0049/214/2/24](https://doi.org/10.1088/0067-0049/214/2/24)
- Stierwalt, S., Besla, G., Patton, D., et al. 2015, *The Astrophysical Journal*, 805, 2, doi: [10.1088/0004-637X/805/1/2](https://doi.org/10.1088/0004-637X/805/1/2)
- Stierwalt, S., Liss, S. E., Johnson, K. E., et al. 2017, *Nature Astronomy*, 1, 0025, doi: [10.1038/s41550-016-0025](https://doi.org/10.1038/s41550-016-0025)
- Wang, F., Yang, J., Fan, X., et al. 2021, *The Astrophysical Journal Letters*, 907, L1, doi: [10.3847/2041-8213/abd8c6](https://doi.org/10.3847/2041-8213/abd8c6)
- Yang, J., Wang, F., Fan, X., et al. 2020, *The Astrophysical Journal Letters*, 897, L14, doi: [10.3847/2041-8213/ab9c26](https://doi.org/10.3847/2041-8213/ab9c26)